



Preparation of CuO nanoparticles via organometallic chelate for the removal of acid red 57 from aqueous solutions

Khlood S. Abou-Melha^a, Gamil A.A. Al-Hazmi^{a,b}, Ismail Althagafi^c, Reem Shah^c, Fathy Shaaban^{d,e}, Nashwa M. El-Metwaly^{c,f}, Ashraf A. El-Bindary^{g,*}

^aChemistry Department, Faculty of Science, King Khalid University, Abha 9004, Saudi Arabia, emails: klsaad@kku.edu.sa (K.S. Abou-Melha), jmarshd@kku.edu.sa (G.A.A. Al-Hazmi)

^bChemistry Department, Faculty of Applied Sciences, Taiz University, Taiz 82, Yemen

^cDepartment of Chemistry, Faculty of Applied Science, Umm-Al-Qura University, Makkah 21421, Saudi Arabia, emails: iithagafi@uqu.edu.sa (I. Althagafi), reem.shah@hotmail.com (R. Shah), nmmohamed@uqu.edu.sa (N.M. El-Metwaly)

^dDepartment of Environment and Health Research, The Custodian of the Two Holy Mosques Institute for Hajj and Umrah Research, Umm Al-Qura University, Makkah 21421, Saudi Arabia, email: ffshaaban@uqu.edu.sa

^eDepartment of Geomagnetic and Geoelectric, national Research Institute of Astronomy and Geophysics, Egypt

^fDepartment of Chemistry, Faculty of Science, Mansoura University, Mansoura 35516, Egypt

^gDepartment of Chemistry, Faculty of Science, Damietta University, Damietta 34517, Egypt, emails: abindary@du.edu.eg/abindary@yahoo.com

Received 5 November 2020; Accepted 22 January 2021

ABSTRACT

Nanoparticles of copper oxide (CuO) were achieved via thermal treatment for Cu(II) organometallic complex at calcination temperature up to 650°C. CuO nanoparticles that synthesized were elucidated by different spectroscopic techniques such as X-ray diffraction, energy-dispersive X-ray spectroscopy. CuO nanoparticles were accepted by scanning electron microscopy analysis as its average diameter was from 15 to 20 nm nanoparticles, and N₂ adsorption–desorption as the Brunauer–Emmett–Teller surface area was originated to be 42.674 m² g⁻¹. Studying the adsorption of acid red 57 (AR57) onto CuO nanoparticles from aqueous, to evaluate the influence of pH, initial dye concentration, dosage, temperature, and contact time. Practical results clarified that the adsorption potential of CuO for AR57 was improved in acidic instead of basic solutions. The kinetics and equilibrium adsorption data were analyzed using the common adsorption models. These outcomes detect that Langmuir isotherm fits with the practical data obtained by a good level. The dye uptake process followed the pseudo-second-order rate expression. The activation energy of adsorption was also evaluated and found to be 30.94 kJ mol⁻¹, indicating that the adsorption is chemisorption. Various thermodynamic limits, such as ΔG, ΔH, and ΔS were determined at various temperatures using adsorption equilibrium constants obtained from the Langmuir isotherm. Thermodynamics of adsorption detect the endothermic and spontaneous nature of such process.

Keywords: CuO nanoparticles; AR57 adsorption; Kinetics; Isotherm; Thermodynamics

* Corresponding author.

1. Introduction

Rivers, oceans, and lakes are getting more and more water disposed of due to a major problem which is water pollution. One of the water pollutants that has gained a great deal of attention is organic dye because of its toxic nature and adverse effects on all life forms [1]. The industry of dyes is one of the significant causes for environmental pollution due to greatly colored waste discharge [2]. Colorants are immune to light, other chemicals, oxidizing agents, and are biologically non-degradable due to its chemical structure, and hence once released into the aquatic environment it is hard to remove [3]. Aquatic life can be affected by the removal of this colored water into receiving waters.

Conventional wastewater treatment methods are very difficult to use in treating dyes from the textile industry due to economic considerations, such as ultrafiltration, coagulation, oxidation, ozonation, reverse osmosis, sedimentation, flotation, precipitation, etc. Removal of contaminants by adsorption has gaining in popularity in recent years because of the proven efficiency of changing wastes to stable forms than the above conventional treatment methods [4]. Copper oxide, has taken great consideration as a result of its attractive potential applications as its uses in an interesting class of crystalline materials [5,6]. The catalytic behavior and selectivity of the nano copper oxide are superior to that of the bulk copper oxide material. Nanoparticle surface modification leads to high surface functionality that increases the exposed surface area, and more significantly, helps to monitor particle agglomeration across time. These could give the nanoparticles excellent adsorption activity of colorants and pesticides [7,8]. Copper oxide (CuO) nanoparticles have been widely considered for many years due to their important roles in catalysis, metallurgy, and high-temperature superconductors. Several preparation methods of CuO nanoparticles have been reported [9,10]. The chemical and physical properties of these materials depend on its composition, structure, phase, shape, and size distribution. Several efforts were exerted to explore the possible implementation of such metal oxide nanoparticles for socio-economic development [11,12].

In this research, we planned to investigate the efficiency of CuO nanoparticles as an adsorbent to eliminate hazardous dye (AR57) from an aqueous solution. As AR57 was anionic dye (acid dye), the treatment of industrial wastewater to remove color from it has become environmentally important. The anionic dyes in the aqueous solution carry a net negative charge due to the sulfonate groups. Therefore, a great demand is to treat these effluent dyes before releasing into an aqueous environment. Also, they have an aromatic structure which makes them more stable and difficult to biodegrade. Systematic characterization of materials as the prepared nanoparticles of CuO was confirmed by means of various techniques. Indexes effect on adsorption process such as adsorbent dosage, initial adsorbate concentration, solution, contact time, pH, and temperature were studied experimentally. The experimental equilibrium adsorption data was analyzed by kinetic and isotherm models. To describe the mechanism of the operation, the thermodynamic parameters were evaluated.

2. Experimental

2.1. Materials and devices

All handled reagents were obtained and used without any further purification from Sigma Aldrich (Germany) and Merck (Germany). A commercial textile dye Acid Red 57 was obtained from Cromatos Società a responsabilità limitata (Italian), a dyes company located in Italy, and was used as received without further purification. Automatic Analyzer CHNS Vario ELIII, Germany, obtained micro-analytical data (C, H, and N). The copper content was estimated using a flame atomic absorption spectrophotometer (model Varian AA240FS) for each stoichiometric measurement. Spectroscopic data of the chelate was obtained using Fourier transform infrared (FTIR) spectrum (KBr discs, 4,000–400 cm^{-1}) by Jasco FTIR-4100 spectrophotometer (Japan). Structural deviations of the as-prepared CuO sample was investigated by X-ray diffraction (XRD) system by a Shimadzu XRD-6000 diffract meter (Shimadzu Corporation, Tokyo, Japan) equipped with Cu $K\alpha$ radiation ($\lambda = 1.54 \text{ \AA}$). At a scanning rate of 0.02° , the 2θ range ranged between 5° and 80° . The values of the crystal structure, space group, and lattice parameters were calculated and optimized using the computer databases CRYSFIRE and CHEKCELL [13]. The HACH LANGE DR5000 (UV-visible spectrophotometer) was used for sample maximum absorbance using 1.0 cm quartz cells. N_2 sorption isotherms were recorded at the boiling temperature of liquid nitrogen (-196°C) on ASAP 2020 (Micrometrics, USA). Before analysis, the particles were exposed to a vacuum (5×10^{-3} torr) at 200°C in order to ensure a clean surface. Brunauer–Emmett–Teller (BET) method was utilized and from which BET surface area and Barrett–Joyner–Halenda (BJH) pore volume were estimated. Scanning electron microscopy (SEM) was utilized to investigate the surface morphology of CuO at accelerating voltages of 20 kV (JEOL-JSM-6510 LV) by using a gold coating examination. The distribution of CuO elements was configured by using energy-dispersive X-ray spectroscopy (EDX) and taken on a Leo1430VP microscope with an operating voltage 5 kV. HANNA instrument pH meter (Romania) (model 211) was used for pH modification.

2.2. Preparation of $[\text{Cu}(\text{L})(\text{CH}_3\text{COO})]2\text{H}_2\text{O}$ chelate

The azo compound of (E)-2-(5-phenyl-4,5-dihydro-1H-pyrazol-3-yl)-4-(phenyldiazenyl)phenol (HL) and its $[\text{Cu}(\text{L})(\text{CH}_3\text{COO})]2\text{H}_2\text{O}$ chelate (Fig. 1) were prepared previously [14] and its purity was checked by elemental analyses and FTIR spectroscopy.

For (HL): yield, 78%, FW: 342.40 g mol^{-1} . Analysis: found: C 73.57%, H 5.28%, and N 16.45%. Calculated for $\text{C}_{21}\text{H}_{18}\text{N}_4\text{O}$: C 73.66%, H 5.28%, and N 16.45%. FTIR ($\nu \text{ cm}^{-1}$) in KBr: 3,418 (OH); 3,325 (NH)_{pyr'}; 1,720 (C=O); 1,595 (C=N)_{pyr'}; and 1,496 (N=N).

For $[\text{Cu}(\text{L})(\text{CH}_3\text{COO})]2\text{H}_2\text{O}$: yield, 75%, FW: 500.0 g mol^{-1} . Analysis: found: C 55.25%, H 4.84%, N 11.21%, and Cu 12.71%. Estimated for $\text{C}_{23}\text{H}_{24}\text{CuN}_4\text{O}_5$: C 55.40%, H 4.74%, N 11.09%, and Cu 12.68%. FTIR ($\nu \text{ cm}^{-1}$) in KBr: 1,580 (C=N)_{pyr'}; 1,558 (COO)_{asym'}; 1,450 (COO)_{sym'}; 690 (Cu–O); and 520 (Cu–N).

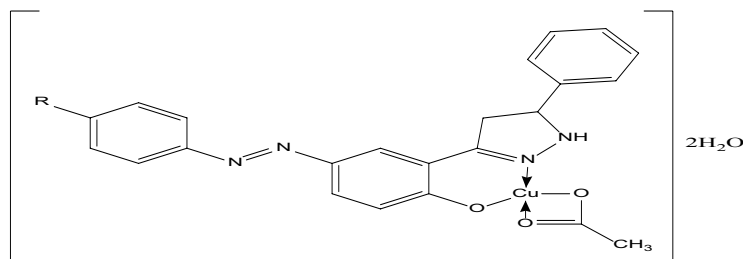


Fig. 1. Structure of Cu(II) chelate (R=H).

2.3. Preparation of CuO nanoparticles

[Cu(L)(CH₃COO)]2H₂O chelate was treated thermally at a calcination temperature of 650°C for 4 h to obtain CuO. In addition, a 200 μm mesh was used to sieve the dried CuO sample in order to obtain small uniform particles. CuO nanoparticles can be produced by this quick and simple method without costly and toxic solvents or complicated equipment.

2.4. Batch adsorption technique

Batch adsorption techniques were performed to study the consequence of limitations such as adsorbent dose, initial dye concentration, contact time, solution pH, and temperature for the removal of AR57 by CuO nanoparticles. Stock solutions of AR57 (1 × 10⁻³ M) were prepared by dissolving an accurate quantity of AR57. Deionized water was used in preparing the stock solutions and also throughout the experimental analysis [15]. Then shaking of 50 mL conical flasks that contain 0.02 g of CuO and 25 mL of dye solutions of anticipated concentration with attuned pH was carried out by using a shaker water bath under a constant speed of 200 rpm. To observe the effect of adsorbent dose on dyes adsorption, different amounts of CuO (varying from 0.01 to 0.10 g) were, respectively, added into the initial concentration of AR57 (1.22 × 10⁻⁴ M) at 25°C and the desired pH until the equilibrium time was reached. Changing pH values from 2 to 12, to investigate the effect of pH on AR57 adsorption and modified to the desired value using 0.1 mol L⁻¹ HCl and 0.1 mol L⁻¹ NaOH solutions. Using centrifuge at 3,000 rpm for 5 min at the end of the adsorption cycle, the supernatant solution was isolated from the adsorbent. Therefore, the residual concentration of dye was spectrophotometrically evaluated by UV-vis spectrophotometer at 512 nm for AR57. Eq. (1) was used to measure the percentage of dye removal (R):

$$R = 100 \frac{(C_0 - C_e)}{C_0} \quad (1)$$

where C₀ (mmol g⁻¹) is the initial dye concentration and C_e (mmol g⁻¹) is the equilibrium dye concentration after time *t*.

For the adsorption isotherm process, dye solutions of different concentrations (8.85 × 10⁻⁵ – 3.63 × 10⁻⁴ M) for AR57 were agitated with 0.02 g of adsorbent until achieving equilibrium. Equilibrium adsorption capacity, *q_e* (mmol dye per g adsorbent) was designed from Eq. (2):

$$q_e = V \frac{(C_0 - C_e)}{m} \quad (2)$$

where C_e (mmol g⁻¹) is the dye concentration at equilibrium, V (L) is the volume of solution, and *m* (mg) is the weight of adsorbent.

The kinetic experiment at constant temperature was similar to that of the equilibrium experiments. Available aqueous samples (5 mL) were obtained from solution at predetermined moments, the liquid was extracted by centrifuge from the adsorbent and the dye concentration in solution was measured spectrophotometrically. Applying Eq. (3), the adsorbed dye quantity at time *t*, *q_t* (mmol g⁻¹) was obtained.

$$q_t = V \frac{(C_0 - C_t)}{m} \quad (3)$$

where C₀ (ppm) is the initial concentration of dye, C_{*t*} (ppm) is the dye concentration at any time *t*, V (L) is the volume of the solution, and *m* (mg) is the mass of the adsorbent.

Then, thermodynamics of the adsorption process indicate that the AR57 adsorption behavior was investigated at 20°C, 25°C, 30°C, 35°C, 40°C, and 45°C with an initial dye concentration 1.22 × 10⁻⁴ M and adsorbent dosage of 0.02 g CuO. The solution was shaken for 30 min at 200 rpm using a shaker water bath, then the absorption was measured spectrophotometrically [16] and *q_t* (mmol g⁻¹) was estimated.

The point of zero charge (pH_{PZC}) was calculated using the method of solid addition. A series of 0.1 M KNO₃ solutions (50 mL each) were prepared and their pH values were adjusted in the range 1–12 by adding 0.1 mol L⁻¹ HCl or 0.1 mol L⁻¹ NaOH. To each solution, 0.1 g of CuO nanoparticles were added and the suspensions and then shaken manually, and the solution was kept for a period of 48 h with intermittent manual shaking. The final pH of the solution was recorded and the difference between initial and final pH (ΔpH) (Y-axis) was plotted against the initial pH (X-axis).

3. Results and discussion

3.1. Characterization of CuO nanoparticles

3.1.1. XRD patterns

The chemical composition of the CuO nanoparticles was analyzed using XRD analysis. The results of XRD

show a number of peaks in the 2θ range of 20° – 80° (Fig. 2). In diffraction pattern, all peaks are well indexed to the monoclinic phase of CuO with space group C2/c, which was confirmed by JCPDS card No. 00-045-0937 [12]. The characteristic peaks located at $2\theta = 32.17^\circ, 35.16^\circ, 38.38^\circ, 38.88^\circ, 48.40^\circ, 53.13^\circ, 58.94^\circ, 61.18^\circ, 65.40^\circ, 66.28^\circ, 67.70^\circ, 68.10^\circ, 72.38^\circ, 74.81^\circ,$ and 76.77° are assigned to (110), (002), (111), (200), (202), (020), (020), (113), (022), (311), (113), (220), (311), (044), and (222) plane orientation of CuO. The main peaks at $2\theta = 35.16^\circ$ and 38.88° of nearly equal intensities corresponding to (002) and (111) planes are the characteristic peaks for the monoclinic phase of pure CuO nanoparticles. The average crystallite size (D , Å) has been estimated from the XRD pattern using the Scherrer's equation (Eq. (4)) [17]. There are no peaks observed for any impurity, indicating the high purity of the sample.

$$D = \frac{K\lambda}{\beta \cos\theta B} \quad (4)$$

where λ is the X-ray wavelength (1.54 \AA), β is the angular width of the peak at half its maximum intensity (full width at half-maximum) corrected for instrumental broadening, B is the maximum of the Bragg diffraction peak, and K is the Scherrer constant (0.9 \AA). The crystallite size of CuO calculated from the high-intensity (002) peak was 17.13 nm (Fig. 2).

3.1.2. BET surface area

BET surface area and BJH pore size of CuO nanoparticles were investigated using N_2 adsorption/desorption measurements at 77 K (Fig. 3). The N_2 adsorption–desorption isotherm of CUO nanoparticles is classified as type III that referred to non-porous solid at $P/P_0 = 0.991$. BET surface area of CuO was created to be $42.674 \text{ m}^2 \text{ g}^{-1}$, assuming a value of 16.2 \AA for N_2 molecule cross-sectional area [12]. The total volume of pore taken at a saturation pressure and expressed as liquid volume, however, is $0.1178 \text{ cm}^3 \text{ g}^{-1}$ and 14.5068 nm in average pore diameter. BJH had a surface area of $61.139 \text{ m}^2 \text{ g}^{-1}$, a pore volume of $0.125 \text{ cm}^3 \text{ g}^{-1}$ and a pore diameter of $D_v(d) 1.656 \text{ nm}$. The external surface area $42.674 \text{ m}^2 \text{ g}^{-1}$ were (calculated on t -plot method), which is advantageous for adsorption application.

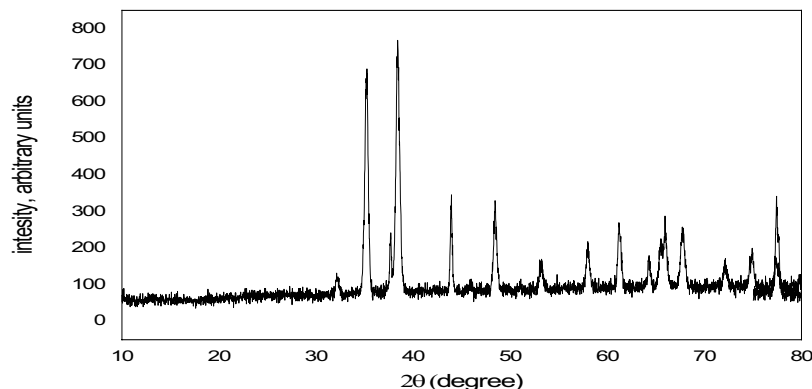


Fig. 2. X-ray diffraction spectra of CuO nanoparticles.

3.1.3. SEM analysis

SEM technique was utilized to examine the morphology of the surface for CuO nanoparticles. Fig. 4 clarifies a uniform development of metal oxide. Higher magnification SEM images show that the cultivated nanostructures have appeared in nanoparticle features that have been interconnected then produced pores and crevices, which creating wide surface areas for fast dye diffusion on the surface of metal oxides [18]. CuO nanoparticles were accepted by SEM analysis as its average diameter was from 15 to 20 nm nanoparticles.

3.1.4. EDX spectroscopy

Energy dispersive X-ray analysis is based on the idea that a particular atomic structure provides each element with a unique collection of peaks on the X-ray spectrum. The elemental composition of CuO nanoparticles was determined by EDX analysis coupled with SEM. Peaks assigned to Cu and O were identified, but no impurity peaks were found, which further identified that the CuO was pure for a long time (Fig. 5) [18].

3.1.5. Optical properties

The energy gap quantity of CuO nanoparticles was evaluated from UV-visible spectroscopy to study the optical

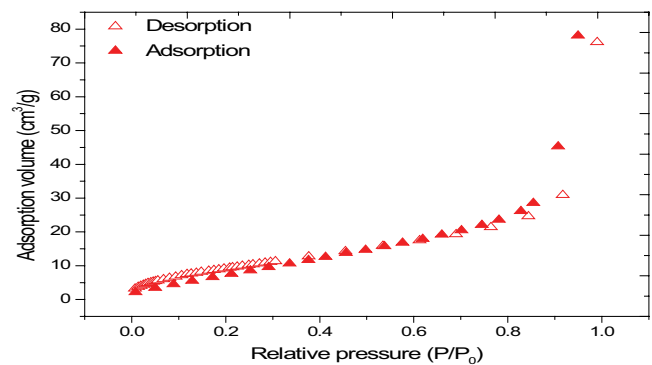


Fig. 3. N_2 sorption isotherm of CuO nanoparticles.

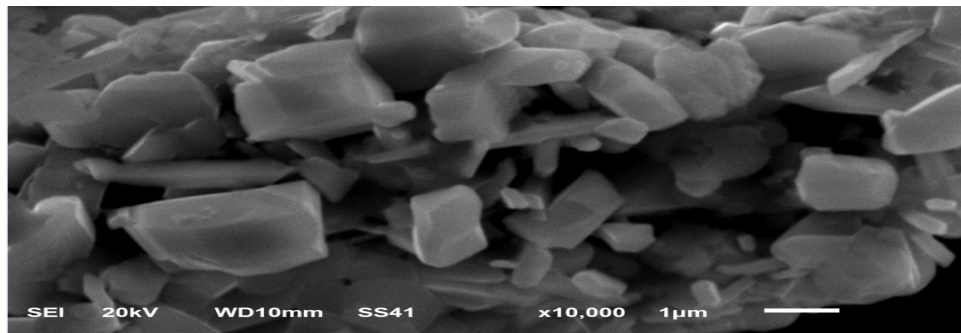


Fig. 4. SEM image of CuO nanoparticles.

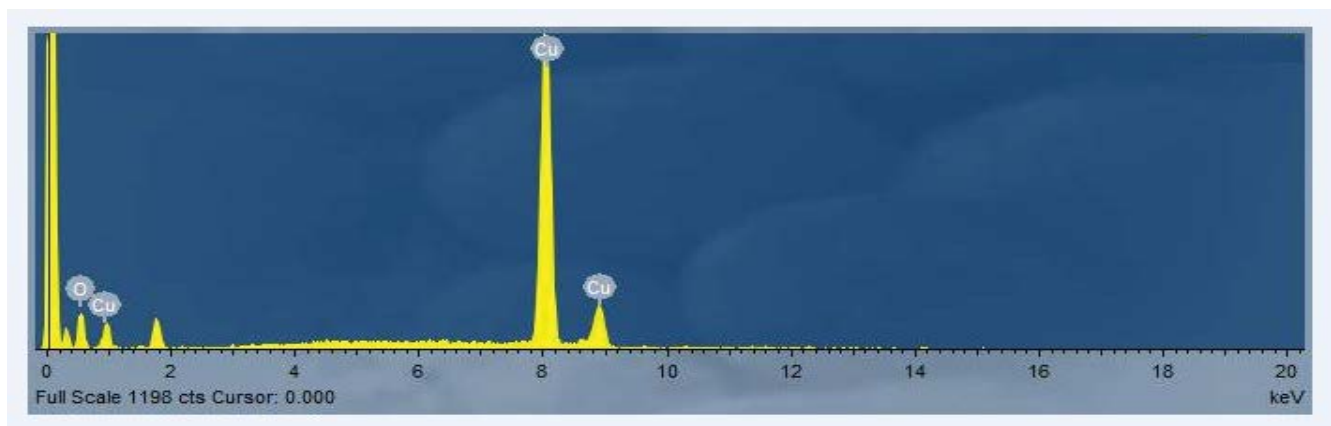


Fig. 5. EDX pattern of CuO nanoparticles.

properties of these particles. Depending on the absorption spectrum of the sample, the bandgap energy of CuO nanoparticles was measured based on Eq. (5):

$$E_g = \frac{1,240}{\lambda_g} \quad (5)$$

where E_g is the energy value of the optical band gap of photocatalyst, λ_g is the wavelength in nm used as the absorption edge. In addition, the bandgap energy was calculated using Tauc's formula [19,20] which clarifies the absorption coefficient relationship as follows (Eq. (6)) [20]:

$$(\alpha h\nu)^{1/n} = B(h\nu - E_g) \quad (6)$$

where α is the absorption coefficient, h is Planck's constant, and ν is the frequency ($\nu = c/\lambda$, λ is the wavelength, c is the light speed). For the allowed direct bandgap the value of n equal to 1/2. Exponent n is dependent on the form of transformation and may have values of 1/2, 2, 3/2, and 3 correspondings to the permitted direct, permitted indirect, prohibited direct, and prohibited indirect transitions [21]. B is a constant and generally called band tailing parameter. Thus, the band gap energy was found 1.10 eV and obtained

graphically from $(\alpha h\nu)^2$ vs. $h\nu$ for direct transition, extrapolating the linear part on the abscissa according to Eq. (6).

3.1.6. Identification for point of zero charge (pH_{PZC})

The zero charge point (pH_{PZC}) was calculated by means of a solid addition process. A series of 0.1 M KNO_3 solutions (50 ML each) were prepared and their pH values were adjusted in the range of 1.0–12.0 by addition of (0.1 or 0.01 mol L^{-1} HCl), or (0.1 or 0.01 mol L^{-1} NaOH). 0.1 g of CuO was applied to each solution and the suspensions were shackled manually, and the solution was held at 25°C for a duration of 48 h with occasional manual shaking. The overall pH of the solution was reported and the difference was plotted against the initial pH (X-axis) between the initial and final pH (ΔpH) (Y-axis).

One of the most important parameters for AR57 sorption was pH, as it determined which ionic species in the adsorbate solution were present and the sorbent surface charge. PZC, which is definite as the pH (pH_{PZC}) at which the positive charges on the surface are equal to the negative charges, was used to determine the surface charge of CuO nanoparticles. CuO's pH_{PZC} was originated to be 7.88. This shows that below this pH, the CuO nanoparticles acquire a positive charge due to the protonation of functional groups and above this pH, a negative charge occurs on the surface of CuO. At $pH < pH_{PZC}$, adsorption

of anionic dyes is preferred where the surface becomes positively charged (Fig. 6) [22].

3.2. Batch experiments

3.2.1. Effect of pH

The pH value of the aqueous solution is a significant limitation in the study of anionic dye adsorption because of its effect on both the ionization of dye molecules and the surface binding sites. The removal of the tested dye AR57 by CuO nanoparticles at altered pH values (2–12) was studied at an initial concentration of 1.22×10^{-4} M for AR57 at 25°C with 0.02 g CuO. The CuO nanoparticles have proved to be an effective adsorbent for the elimination of this dye and the most actual pH was 3 for AR57 (Fig. 7). The positive charge on the oxide or solution interface decreases as the pH of the solution is elevated, and the adsorbent surface becomes negatively charged. On the other hand, the concentration of OH⁻ ions and ionic repulsion between the negatively charged surface and the anionic dye molecules may be due to lower adsorption at elevated pH values [23]. Consequently and at such pH values, there are also no exchangeable anions on the outer surface of the adsorbent then the adsorption decreases. Thus, at $\text{pH} < \text{pH}_{\text{pzc}}$, where the surface is positively charged, the adsorption of anionic dyes is favorable.

3.2.2. Effect of adsorbent dosage

The adsorption of AR57 to CuO nanoparticles sorbent was studied by altering the adsorbent range 0.01–0.1 g per 25 mL, 1.22×10^{-4} M, and pH 3 for AR57 at adsorbate concentrations. Outcomes in Fig. 8a show the adsorption potential of AR57 as a purpose of the quantity of adsorbent. Adsorption potential was found to decrease from 1.06 to 0.28 mmol g⁻¹ for AR57 and increases from 0.01 to 0.1 g per 25 mL as the dose of CuO increases. The dosage effect on the equilibrium concentration (C/C_0) of AR57 by the copper oxide sorbent is shown in Fig. 8b. The balance concentration of AR57 is reduced as the dosage increases, due to the rise in the adsorbent surface area of the adsorbent.

3.2.3. Effect initial concentration (C_0)

The effect of the initial AR57 concentration on CuO nanoparticles was investigated with a dye concentration of $8.85 \times 10^{-5} - 3.63 \times 10^{-4}$ M and an adsorbent dose of 0.02 g. With an increase in the initial dye concentration of AR57, the removal percentage decreased. The percentage decrease in adsorption is due to saturation at higher concentrations of AR57 of the active binding sites of CuO.

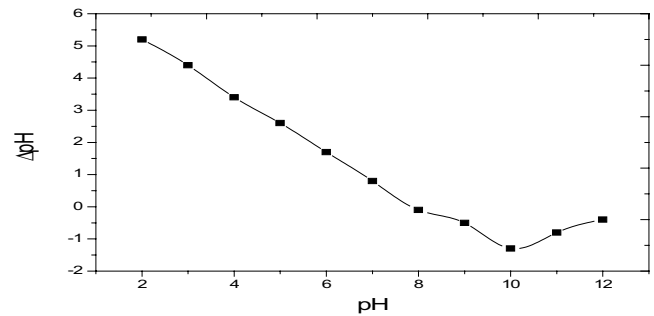


Fig. 6. Relation between the initial pH and ΔpH of CuO nanoparticles.

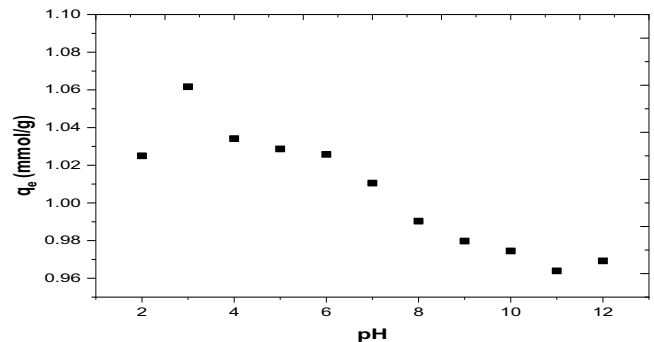


Fig. 7. pH effect on AR57 adsorption using CuO nanoparticles as adsorbent ($T: 25^\circ\text{C}$, $C_0: 1.22 \times 10^{-4}$ M).

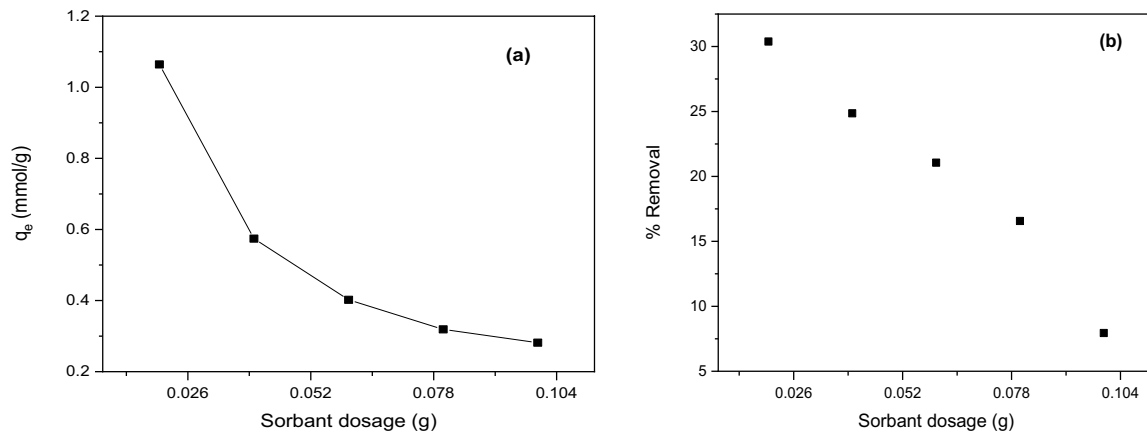


Fig. 8. Effect of sorbent dose (SD) on AR57 adsorption using CuO nanoparticles: (a) sorption capacity vs. SD and (b) % Removal vs. SD ($C_0: 1.22 \times 10^{-4}$ M, $T: 25^\circ\text{C}$, and pH 3).

3.2.4. Adsorption isotherms

The experiments were performed at pH 3 and 1.22×10^{-4} M for AR57, with an adsorbent dose of 0.02 g at 25°C. Isotherm studies provide valuable insights by clarifying the distribution of adsorbate during the adsorption equilibrium between solid and solution level, and adsorption isotherms show the actions of adsorbate how to communicate with the adsorbent. Adsorption isotherms describe equilibrium studies that give the ability of the adsorbent and adsorbate, which is typically the ratio amongst the amount adsorbed and that remained in solution at equilibrium at fixed temperature [24,25]. To consider the equilibrium adsorption of compounds from solutions such as Langmuir [26], Freundlich [27], Dubinin–Radushkevich [28], and Temkin [29], various isothermal models have been used.

The linear and nonlinear forms of Langmuir, Freundlich, Dubinin–Radushkevich, and Temkin isotherm models and their limitations are shown in Table 1. Where q_e the adsorbed amount of dye at equilibrium concentration (mmol g^{-1}), q_{mL} is the maximum sorption capacity (corresponding to the saturation of the monolayer, mmol g^{-1}) and K_L is the Langmuir binding constant which is related to the energy of sorption (L mmol^{-1}), C_e is the equilibrium concentration of dyes in solution (M). K_F (mmol g^{-1}) ($\text{L mmol}^{-1/n}$) and n are the Freundlich constants related to sorption capability and intensity, respectively. K_{DR} ($\text{J}^2 \text{mol}^{-2}$) is a constant belongs to sorption energy, q_{DR} (mmol g^{-1}) is the theoretical saturation capability, ϵ ($\text{J}^2 \text{mol}^{-2}$) is the Polanyi potential. R ($8.314 \text{ J mol}^{-1} \text{ K}^{-1}$) is the gas constant, T is the temperature where the adsorption occurs, A_T (L mg^{-1}) is the Temkin isotherm constant, b_T (J mol^{-1}) is Temkin constant in relation to heat of adsorption.

The isotherm model of Langmuir was found to be the most effective model for defining the isotherm for AR57 dye adsorption onto the CuO sorbent (Figs. 9 and 10). However, the Freundlich lines departed from the experimental data points from the isothermal fitting. The isotherm fitting was plotted on the basis of the nonlinear equations using

the model constant parameters obtained from the linear equation plot analysis. The Langmuir model provided the high coefficient of determination $R^2 = 0.9999$ for AR57.

In addition, the q_m determined from the Langmuir isotherm was similar to the experimental q_{max} . Analysis of isotherm parameters proposed by Dubinin–Radushkevich was determined (Table 1). Concerning the effect of the porous structure of sorbent and the energy involved in the sorption process, this isotherm was created. The results of Dubinin–Radushkevich isotherm are reported in Table 1 and Fig. 10. The mean sorption energy value is $30.94 \text{ kJ mol}^{-1}$. This is reliable in relation to the proposed chemisorption process. Indeed, 8 kJ mol^{-1} is commonly accepted as the limit energy for separation, physical (below 8 kJ mol^{-1}), and chemical sorption (up to 8 kJ mol^{-1}).

3.2.5. Adsorption kinetics and mechanism studies

The analysis of adsorption kinetics explains the solute uptake rate and obviously this rate influences the residence time of adsorbate uptake at the solid–solution interface. The rate of removal of tested dye by adsorption was rapid initially with time increased and then slowed progressively until it reached an equilibrium above which there was a substantial increase in the rate of removal. At 100 min, the maximum adsorption was observed and is thus set as the time of equilibrium [11].

In order to determine the adsorption kinetics of AR57 dye on CuO, according to the below kinetic model equations, the pseudo-first-order and pseudo-second-order kinetic models were used to match the experimental results.

The pseudo-first-order rate expression of Lagergren [30] is given as Eq. (7):

$$\log(q_e - q_t) = \log q_e - k_1 t \quad (7)$$

The pseudo-second-order kinetic model [31] is expressed as Eq. (8):

Table 1
Isotherms and their linear forms for the adsorption of AR57 onto CuO nanoparticles

Isotherm	Equation	Value of parameters	
Langmuir	$\frac{C_e}{q_e} = \frac{1}{q_m K_L} + \frac{C_e}{q_m}$	The constants q_m and K_L are calculated by the plot of C_e/q_e vs. C_e with slope $1/q_m$ and intercept $1/(q_m K_L)$	$q_{m,\text{exp}}$ (mmol g^{-1}) 1.2459
			q_m (mmol g^{-1}) 1.256
			K_L (L mmol^{-1}) 248,387.968
			R^2 0.9999
Freundlich	$\ln q_e = \ln K_F + \frac{1}{n} \ln C_e$	K_F and n can be calculated from a linear plot of $\ln q_e$ vs. $\ln C_e$	n 22.9357
			K_F (mmol g^{-1}) ($\text{L mmol}^{-1/n}$) 0.5014
			R^2 0.539
Dubinin–Radushkevich	$\ln q_e = \ln Q_{\text{DR}} - K_{\text{DR}} \epsilon^2$	The slope of the plot of $\ln q_e$ vs. ϵ^2 gives K_{DR} ($\text{mol}^2 \text{kJ}^{-2}$) and the intercept yields the adsorption capacity, Q_{DR} (mmol g^{-1})	Q_{DR} 0.346
			K_{DR} ($\text{J}^2 \text{mol}^{-2}$) $-4.9\text{E-}10$
			E_a (kJ mol^{-1}) 31.94
			R^2 0.74
Temkin	$q_e = \beta_T \ln K_T + \beta_T \ln C_e$	The parameters β and K_T are the Temkin constants that can be determined by the plot of q_e vs. $\ln C_e$	b_T (L mol^{-1}) 49,413.08
			A_T (kJ mol^{-1}) 31.29
			R^2 0.7139

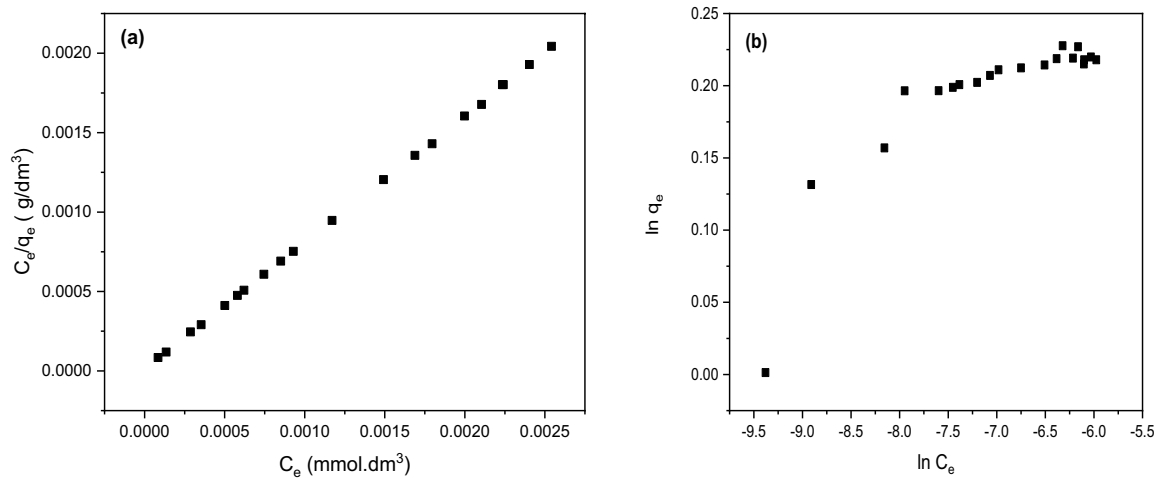


Fig. 9. Linearized isothermal sorption plots for AR57: (a) Langmuir equation and (b) Freundlich equation.

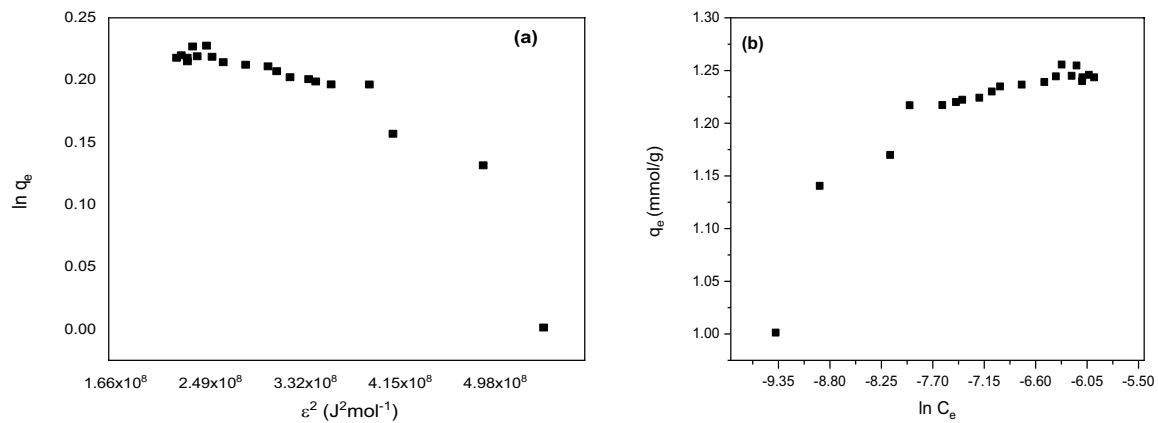


Fig. 10. Linearized isothermal sorption plots for AR57: (a) Dubbin–Radushkevich equation and (b) Temkin model.

$$\frac{t}{q_t} = \frac{1}{k_2 q_2^2} + \frac{1}{q_2 t} \tag{8}$$

where q_t is the amount of dye adsorbed (mmol g^{-1}) at various times t , q_e is the maximum adsorption capacity (mmol g^{-1}) for pseudo-first-order adsorption, k_1 is the pseudo-first-order rate constant for the adsorption process (min^{-1}), q_2 is the maximum adsorption capacity (mmol g^{-1}) for the pseudo-second-order adsorption, k_2 is pseudo-second-order adsorption ($\text{g mol}^{-1} \text{min}^{-1}$) rate constant. The straight-line plots of $\log(q_e - q_t)$ vs. t for pseudo-first-order reaction and t/q_t vs. t for pseudo-second-order reaction (Figs. 11 and 12). The adsorption of AR57 dye onto CuO have also been tested to obtain the rate parameters. The k_1 , k_2 , q_1 , q_2 , and correlation coefficients, r_1^2 and r_2^2 for the dye under different temperatures were evaluated from these plots and tabulated in Table 2.

So, neither pseudo-first-order nor pseudo-second-order model can classify the diffusion mechanism; then the kinetic results were further analyzed for diffusion mechanism by using intra-particle diffusion model. The effect on adsorption of intra-particle diffusion constant (internal surface and pore diffusion) can be calculated by Eq. (9):

$$q_t = k_{id} t^{1/2} + I \tag{9}$$

where I is the intercept and k_{id} is the rate constant of intra-particle diffusion ($\text{mg g}^{-1} \text{min}^{0.5}$) which is determined from the linear plot of q_t vs. $t^{1/2}$ (Figs. 11 and 12) and it is usually used to compare mass transfer rates. Accordingly, if intra-particle diffusion is involved in the adsorption process, the plot of uptake, q_t vs. the square root of time, $t^{1/2}$ should be linear and if these lines move through the origin, then the rate-control stage is intra-particle diffusion. The intra-particle diffusion rate constant and intercept values are displayed in Table 2 [24,25].

The Elovich equation is used for general application to chemical adsorption. For certain chemical adsorption processes, the equation has been applied satisfactorily and has been found to cover a wide range of slow adsorption speeds. Systems having heterogeneous nature of the adsorbing surface, Eq. (10) as the same equation is also valid and expressed as:

$$q_t = \left(\frac{1}{\beta}\right) \ln(\alpha\beta) + \left(\frac{1}{\beta}\right) \ln t \tag{10}$$

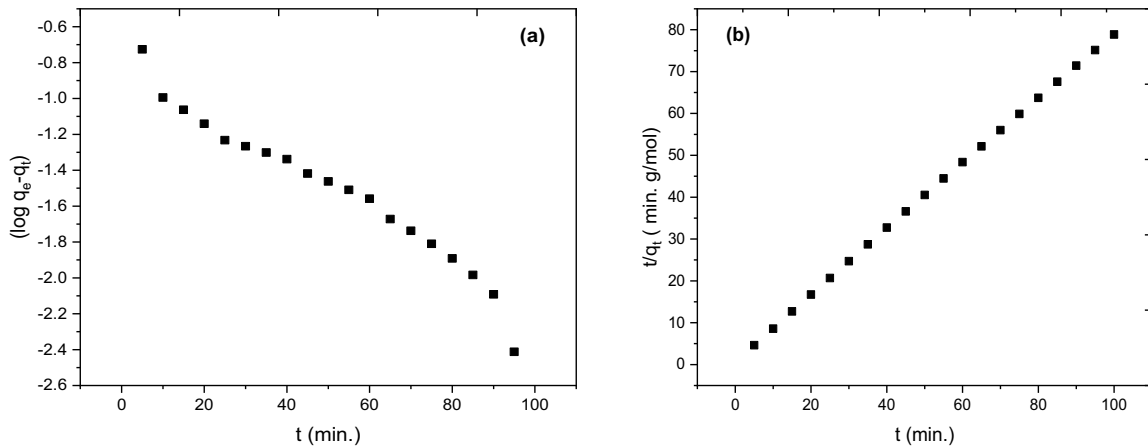


Fig. 11. Modeling for uptake kinetics of AR57 with: (a) pseudo-first-order rate expression and (b) pseudo-second-order rate expression.

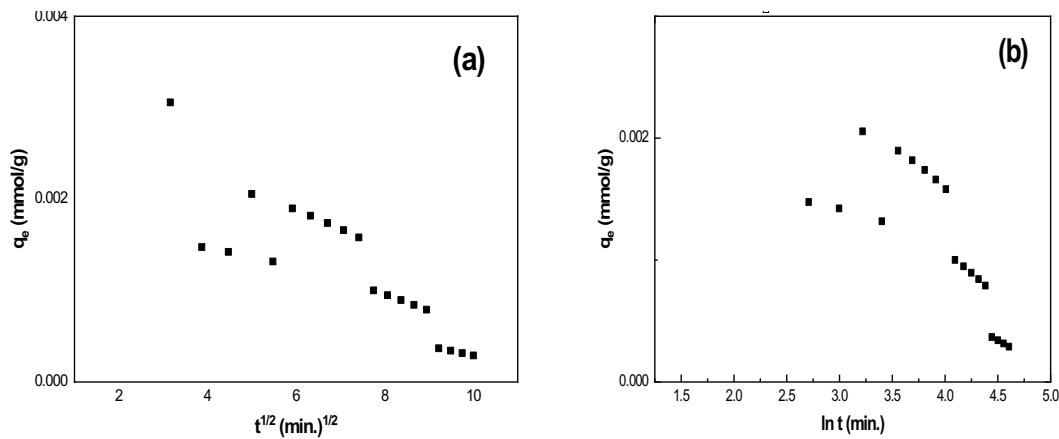


Fig. 12. Uptake kinetics modeling for AR57 with: (a) simplified model of resistance to intraparticle diffusion (Morris and Weber equation) and (b) Elovich equation.

Table 2

Kinetic parameters and their correlation coefficients for the adsorption of AR57 onto CuO nanoparticles.

Model	Equation	Value of parameters
Pseudo-first-order kinetic	$\log(q_e - q_t) = \log q_e - \left(\frac{K_1}{2.303}\right)t$	K_1 (min^{-1}) 0.0145 q_e (mmol g^{-1}) -0.0145 R^2 0.95476
Pseudo-second-order kinetic	$\frac{t}{q_t} = \frac{1}{K_2 q_e^2} + \frac{t}{q_e}$	Values of K_2 and q_e for different initial concentrations of dye were calculated from the slope and intercept of the linear plot of t/q_t vs. t K_2 ($\text{g mg}^{-1} \text{min}^{-1}$) 0.536 q_e (mmol g^{-1}) 1.27 R^2 0.99987
Intraparticle diffusion	$q_t = K_{\text{dif}} t^{1/2} + X$	The parameters K_{dif} and C were determined from the linear plot of q_t vs. $t^{1/2}$ K_{dif} ($\text{mg g}^{-1} \text{min}^{1/2}$) -0.0574 X (mg g^{-1}) 0.438 R^2 0.2287
Elovich	$q_t = \frac{1}{\beta} \ln(\alpha\beta) + \frac{1}{\beta} \ln t$	The constants α and β were obtained from the slope and intercept of a line plot of q_t vs. $\ln t$ β (g mg^{-1}) -5.26 α ($\text{mg g}^{-1} \text{min}^{-1}$) 2.187 R^2 0.395
Experimental data		$q_{e,\text{exp}}$ (mmol g^{-1}) 1.268

where α is the chemical adsorption rate ($\text{mg mg}^{-1} \text{min}^{-1}$) and β is a coefficient in relation with the extension of covered surface and activation energy of chemical adsorption (g mg^{-1}). Plot of q_t vs. $\ln t$ gave a linear relationship with a slope of $(1/\beta)$ and an intercept of $(1/\beta) \ln(\alpha\beta)$. The $1/\beta$ value the $1/\beta$ value reflects the number of sites available for adsorption whereas the value of $(1/\beta) \ln(\alpha\beta)$ indicates the adsorption quantity when $\ln t$ equal to zero.

Upon comparison among the kinetic models, the R^2 values of the pseudo-second-order kinetic model (0.99987) is much higher than those of pseudo-first-order kinetic model (0.95476) for AR57, implying that the kinetics of dye adsorption follows the pseudo-second-order kinetic model. The coefficient of determination supports this consideration, and the $q_{e,\text{calc}}$ value from the kinetic pseudo-second-order model is in good agreement with the practical outcomes. The rate-limiting step in this adsorption process may be chemisorption involving strong forces through the sharing or exchanging of electrons between sorbent and sorbate. The intra-particle diffusion curve gives multi-linearity, it does not pass through the origin. The intra-particle diffusion kinetic model ($R^2 = 0.2287$) for AR57 was considered from the slope of the corresponding second linear region Figs. 11 and 12. Only in the initial stages of adsorption (initial sharp increase) is the external resistance to mass transfer surrounding the particles substantial [32]. The second linear component is the process of gradual adsorption with intra-particle diffusion regulation. If the plots do not pass through the origin, it means that the diffusion of the pore is not the sole rate-limiting stage, but the adsorption rate can also be regulated by other kinetic models, both of which can operate simultaneously. The Elovich equation assumes that the adsorbent's active sites are heterogeneous and, thus, show different chemisorption activation energies. When increasing the concentration of dye, it was observed that the constant α (related to the rate of chemisorption) increased and the constant β (related to the surface coverage) decreased (Table 2), which is owing to the decrease in the available adsorption surface for the adsorbates. Therefore, by increasing the concentration, within the range studied, the rate of chemisorption can be increased [33]. Therefore, by the pseudo-second-order kinetic model, the adsorption kinetics can be satisfactorily approximated, based on the assumption that chemisorption involving electrostatic forces may be the rate-limiting stage through the sharing or exchange of electrons between the adsorbent and the adsorbate [34].

3.2.6. Effect of temperature

With a view to practical application, the impact of temperature on adsorption should be investigated. It can be

seen from Fig. 13 that with the rise in temperature from 293 to 318 K, the adsorption potential of AR57 increases marginally from 1.06 to 1.22 mmol g^{-1} . This activity confirms that it is endothermic to the adsorption mechanism of AR57 on CuO nanoparticles. This finding can be due to an increase in the mobility of dye molecules and the rate of diffusion of adsorbent molecules at increasing temperatures across the surface of the adsorbent, leading to an increase in the ability of the adsorbent.

Thermodynamic parameters were calculated to evaluate the thermodynamic feasibility of the process using the following equations (Eqs. (11) and (12)) [35,36]:

$$\ln K_c = \frac{\Delta S}{R} - \frac{\Delta H}{RT} \quad (11)$$

$$\Delta G = -RT \ln K_c \quad (12)$$

where K_c is the distribution coefficient for the adsorption, ΔH is the enthalpy change, ΔS is the entropy change, ΔG is the Gibbs's free energy change, R is the gas constant, T is the absolute temperature. ΔH and ΔS were calculated from the slope and intercept of the linear plot of $\ln K_c$ vs. $1/T$ (Fig. 13). Once these two parameters were obtained, ΔG was determined. The negative value of ΔH confirmed the endothermic nature of AR57 adsorption by CuO nanoparticles [10]. The values of ΔG were negative at all temperatures, demonstrating the thermodynamic feasibility and the spontaneity of the adsorption process. The adsorption was associated with a positive value of ΔS (Table 3).

3.2.7. Effect of ionic strength (addition of NaCl)

The effect of chloride ions on Acid Red 57 removal was examined, by the addition of increasing concentrations of NaCl (from 10 to 40 g L^{-1} , C_0 : $1.22 \times 10^{-4} \text{M}$, and sorbent dosage: 0.02 g, 25 mL) for AR57. Concerning the current adsorbents, increasing the amount of NaCl leads to slight decreases in sorption capability: the sorption capacity decreases by about 20%, when NaCl concentration reaches 20 g L^{-1} (Fig. 14). This is possibly due to the competitive effect of chloride anions in contact with the sorption sites against AR57 anions. It is interesting that even when the NaCl concentration exceeds 40 g L^{-1} , the decrease in the adsorption capacity decreases by 1.5%, suggesting that a high adsorption capacity is retained even under these drastic conditions.

3.2.8. Desorption studies

The ability for regeneration and stability of adsorbent are the two influential factors affecting on the practical

Table 3
Standard enthalpy, entropy, and free energy changes for AR57 adsorption on CuO nanoparticles

R^2	ΔH (kJ mol^{-1})	ΔS ($\text{J mol}^{-1} \text{K}^{-1}$)	T_0 (K)	$-\Delta G$ (kJ mol^{-1})				
				293 K	298 K	303 K	308 K	318 K
0.999	17.34	65.92	262.49	36.69	37.02	37.35	37.68	38.5

application of the adsorbent [37]. We have now compared the adsorption capacity of CuO for three-consecutive adsorption-desorption cycles. The investigated sorbent CuO was washed with ethanol several times till colorless and then with distilled water [38]. The colorless product of CuO was dried at 60°C for 24 h to a constant weight. After regeneration the adsorbent ready for the second run of uptake. The regeneration efficiency for each adsorption/desorption cycle was found to be 97.6%, 92.5%, and 68.6% for AR57. This can be due to blocking of adsorption sites of CuO. We have also characterized by XRD of the CuO material after three cycle test and found that the crystallinity and structure remain intact (Fig. 15). This result shows that the CuO nanoparticles are having good reusability characteristic [39]. The efficiency of regeneration was calculated using Eq. (13):

$$\text{Regeneration efficiency (\%)} = \frac{\text{Total adsorption capacity in the second run}}{\text{Total adsorption capacity in the first run}} \times 100 \quad (13)$$

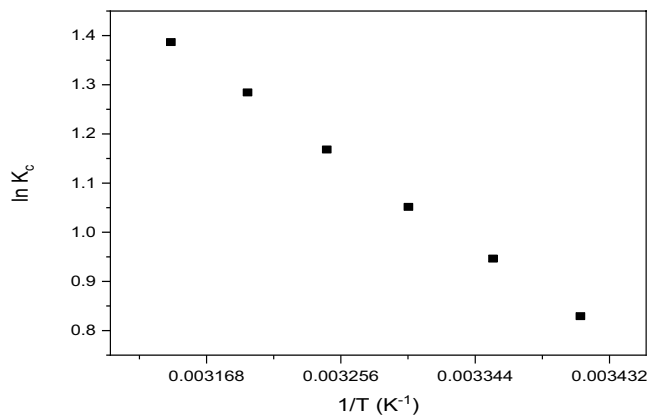


Fig. 13. Van't Hoff plots for AR57 adsorption onto the CuO nanoparticles adsorbent.

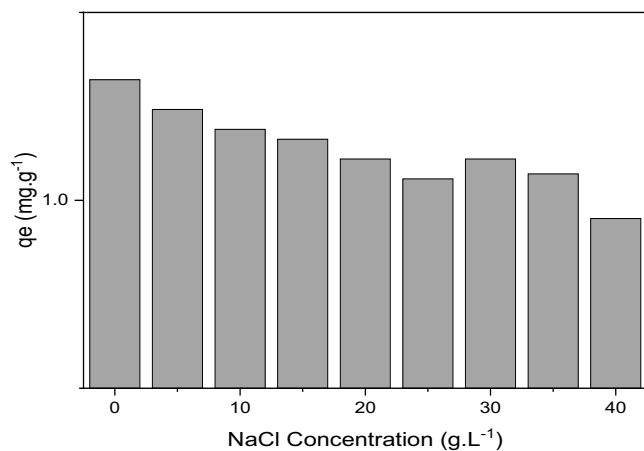


Fig. 14. Influence of NaCl on AR57 adsorption onto CuO nanoparticles (C_0 : 1.2×10^{-4} M, initial pH 3, T : 25°C, and sorbent dosage: 0.02 g, 25 mL).

3.2.9. Comparison with other adsorbents

Comparison of the maximum AR57 adsorption capacities using CuO as an adsorbent with that of the other previously reported adsorbents has been done and presented in Table 4. It shows that CuO possesses a high adsorption capacity for AR57.

4. Conclusions

The adsorption activity of CuO nanoparticles was examined for the elimination of dye solutions such as AR57. CuO nanoparticles were synthesized by calcination of Cu(II) chelate at 650°C. Various techniques have characterized the synthesized CuO nanoparticles, for example, XRD, SEM, and EDX measurements. Under different conditions, the adsorption of AR57 was systematically investigated. Anionic dye (AR57) adsorption was found to be highly dependent on pH, temperature, and contact time. At pH 3 for AR57, complete removal could be achieved. The adsorption of AR57 dye was endothermic as the dye removal capacity increase with an increase in the temperature due to the increase of mobility of dye molecules. The Langmuir isotherm model was found to be the most suitable model for describing the isotherm for adsorption of both AR57 dyes on CuO sorbent. In addition, the q_m calculated from the Langmuir isotherm was close to the experimental q_{max} . The kinetic model of the pseudo-second-order corresponds very well with the complex behavior of the AR57 adsorption to CuO. In addition, thermodynamic parameters such as ΔG , ΔH , and ΔS during the adsorption

Table 4
Adsorption capacity (q_m) of various adsorbents for the AR57 dye

Adsorbent	q_m (mg g ⁻¹)	Reference
Surfactant-modified sepiolite	425	[40]
Sepiolite	134.6	[41]
HTAB-modified sepiolite	307.4	[33]
Acid activated bentonite	416.3	[42]
CuO	691.2	This work

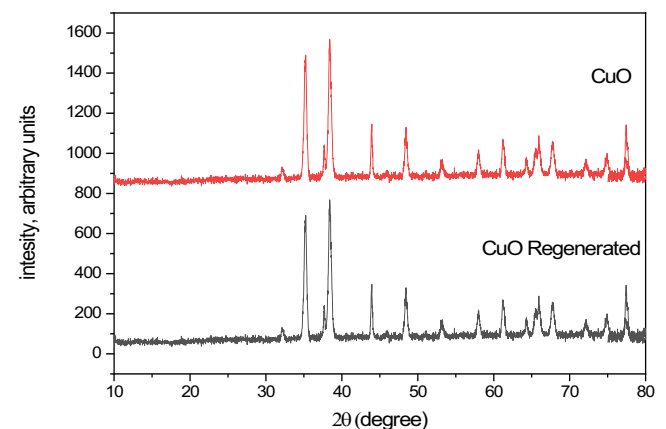


Fig. 15. X-ray diffraction spectra of CuO and CuO regenerated.

process are suggested that the adsorption of AR57 dye on CuO nanoparticles is of a spontaneous and endothermic nature which is favored at a higher temperature and occurs by physical adsorption. Further studies would also be needed to excavate the full potential of CuO for extracting AR57 from real industrial wastewater samples.

Data availability statement

The data that support the findings of this study are available from the corresponding author upon reasonable request.

Acknowledgments

The authors extend their gratitude to King Khalid University's Deanship of Scientific Research for supporting this work through the Grant Number Research Groups Scheme (R.G.P1/236/41).

References

- [1] W. Zou, L. Gong, M. Pan, Z. Zhang, C. Sun, H. Zeng, Effect of salinity on adsorption and interaction forces of hydrophobically modified polyacrylamide on silica and alumina surfaces, *Miner. Eng.*, 150 (2020), doi: 10.1016/j.mineng.2020.106280.
- [2] G. Yang, N. Song, F.G. Deng, J. Liang, Q. Huang, J.B. Dou, Y.Q. Wen, M.Y. Liu, X.Y. Zhang, Y. Wei, Direct surface functionalization of graphene oxide with ionic liquid through gamma ray irradiation induced radical polymerization with remarkable enhanced adsorption capacity, *J. Mol. Liq.*, 306 (2020), doi: 10.1016/j.molliq.2020.112877.
- [3] L. Li, Z.N. Shi, H.Y. Zhu, W. Hong, F.W. Xie, K.K. Sun, Adsorption of azo dyes from aqueous solution by the hybrid MOFs/GO, *Water Sci. Technol.*, 73 (2016) 1728–1737.
- [4] K.Z. Al-Wakeel, H. Abd El Monem, M.M.H. Khalil, Removal of divalent manganese from aqueous solution using glycine modified chitosan resin, *J. Environ. Chem. Eng.*, 3 (2015) 179–186.
- [5] B. Zhang, Y. Wu, L. Cha, Removal of methyl orange dye using activated biochar derived from pomelo peel wastes: performance, isotherm, and kinetic studies, *J. Dispersion Sci. Technol.*, 41 (2020) 125–136.
- [6] M.S. Frost, The response of citrate functionalised gold and silver nanoparticles to the addition of heavy metal ions, *Colloids Surf., A*, 518 (2017) 15–24.
- [7] M.N. Asl, N.M. Mahmodi, P. Teymouri, B. Shahmoradi, R. Rezaee, A. Maleki, Adsorption of organic dyes using copper oxide nanoparticles: isotherm and kinetic studies, *Desal. Water Treat.*, 57 (2016) 25278–25287.
- [8] N. Begletsova, Chemical synthesis of copper nanoparticles in aqueous solutions in the presence of anionic surfactant sodium dodecyl sulfate, *Colloids Surf., A*, 552 (2018) 75–80.
- [9] Saruchi, P. Thakur, V. Kumar, Kinetics and thermodynamic studies for removal of methylene blue dye by biosynthesize copper oxide nanoparticles and its antibacterial activity, *J. Environ. Health Sci. Eng.*, 17 (2019) 367–376.
- [10] K.Y. Kumar, S. Archana, T.N.V. Raj, B.P. Prasana, M.S. Raghu, H.B. Muralidhara, Superb adsorption capacity of hydrothermally synthesized copper oxide and nickel oxide nanoflakes towards anionic and cationic dyes, *J. Sci.: Adv. Mater. Dev.*, 2 (2017) 183–191.
- [11] Z. Liang, Z. Zhao, T. Sun, W. Shi, F. Cui, Enhanced adsorption of the cationic dyes in the spherical CuO/meso-silica nano composite and impact of solution chemistry, *J. Colloids Interface Sci.*, 485 (2016) 192–200.
- [12] M.P. Geetha, P. Pratheeksha, B.K. Subrahmanya, Development of functionalized CuO nanoparticles for enhancing the adsorption of methylene blue dye, *Cogent Eng.*, 7 (2020), doi: 10.1080/23311916.2020.1783102.
- [13] S. Dursun, S.N. Koyuncu, I.C. Kaya, G.G. Kaya, V. Kalem, H. Akyildiz, Production of CuO-WO₃ hybrids and their dye removal capacity/performance from wastewater by adsorption/photocatalysis, *J. Water Process Eng.*, 36 (2020), doi: 10.1016/j.jwpe.2020.101390.
- [14] I.M. El-Deen, A.F. Shoair, M.A. El-Bindary, Synthesis, structural characterization, molecular docking and DNA binding studies of copper complexes, *J. Mol. Liq.*, 249 (2018) 533–545.
- [15] N. Hassan, A. Shahat, A. El-Daidamony, M.G. El-Desouky, A.A. El-Bindary, Synthesis and characterization of ZnO nanoparticles via zeolitic imidazolate framework-8 and its application for removal of dyes, *J. Mol. Struct.*, 1210 (2020), doi: 10.1016/j.molstruc.2020.128029.
- [16] N. Hassan, A. Shahat, A. El-Daidamony, M.G. El-Desouky, A.A. El-Bindary, Mesoporous iron oxide nano spheres for capturing organic dyes from water sources, *J. Mol. Struct.*, 1217 (2020), doi: 10.1016/j.molstruc.2020.128361.
- [17] A.L. Patterson, The Scherrer formula for X-ray particle size determination, *Phys. Rev.*, 56 (1939) 978–982.
- [18] A. Fouda, S.S. Salem, A.R. Wassel, M.F. Hamza, T.I. Shabeen, Optimization of green biosynthesized visible light active CuO/ZnO nano-photocatalysts for the degradation of organic methylene blue dye, *Heliyon*, 6 (2020), doi: 10.1016/j.heliyon.2020.e04896.
- [19] X. Zheng, W. Fu, F. Kang, H. Peng, J. Wen, Enhanced photo-Fenton degradation of tetracycline using TiO₂-coated α -Fe₂O₃ core-shell heterojunction, *J. Ind. Eng. Chem.*, 68 (2018) 14–23.
- [20] J.I. Pankove, *Optical Process in Semiconductors*, Prentice-Hall, New Jersey, 1971.
- [21] H.A. Kiwaan, T.M. Atwee, E.A. Azab, A.A. El-Bindary, Photocatalytic degradation of organic dyes in the presence of nanostructured titanium dioxide, *J. Mol. Struct.*, 1200 (2020), doi: 10.1016/j.molstruc.2019.127115.
- [22] A.A. El-Bindary, S.M. El-Marsafy, A.A. El-Maddah, Enhancement of the photocatalytic activity of ZnO nanoparticles by silver doping for the degradation of AY99 contaminants, *J. Mol. Struct.*, 1191 (2019) 76–84.
- [23] B. Ahmed, A. Rizvi, A. Zaidi, M.S. Khan, J. Misarrat, Understanding the phyto-interaction of heavy metal oxide bulk and nanoparticles: evaluation of seed germination, growth, bioaccumulation, and metallothionein production, *RSC Adv.*, 9 (2019) 4210–4225.
- [24] K.Z. Elwakeel, A.A. El-Bindary, A.Z. El-Sonbati, A.R. Hawas, Magnetic alginate beads with high basic dye removal potential and excellent regeneration ability, *Can. J. Chem.*, 95 (2017) 807–815.
- [25] A.K. Prajapati, M.K. Mondal, Comprehensive kinetic and mass transfer modeling for methylene blue dye adsorption onto CuO nanoparticles loaded on nanoporous activated carbon prepared from waste coconut shell, *J. Mol. Liq.*, 307 (2020), doi: 10.1016/j.molliq.2020.112949.
- [26] I. Langmuir, The adsorption of gases on plane surfaces of glass, mica and platinum, *J. Am. Chem. Soc.*, 40 (1918) 1361–1403.
- [27] H. Freundlich, W. Heller, The adsorption of cis- and trans-azobenzene, *J. Am. Chem. Soc.*, 61 (1939) 2228–2230.
- [28] M.M. Dubinin, E. Zaverina, L. Radushkevich, Sorption and structure of active carbons. I. Adsorption of organic vapors, *Z. Fiziches. Khim.*, 21 (1947) 1351–1362.
- [29] M. Temkin, V. Pyzhev, Recent modifications to Langmuir isotherms, *Acta Physicochim. URSS*, 40 (1940) 217–222.
- [30] S.K. Lagergren, About the theory of so-called adsorption of soluble substances, *Kungl. Svens. Vetenskapsakad. Handl.*, 24 (1898) 1–39.
- [31] Y.-S. Ho, G. McKay, Sorption of dye from aqueous solution by peat, *Chem. Eng. J.*, 70 (1998) 115–124.
- [32] D. Karatas, D. Senol-Arslan, O. Ozdemir, Experimental and atomic modeling of the adsorption of acid azo dye 57 to sepiolite, *Clays Clay Miner.*, 66 (2018) 426–437.
- [33] V. Muinde, J.M. Onyari, B.M. Wamalwa, J. Wabomba, R. Nthumbi, Adsorption of malachite green from aqueous

- solutions onto rice husks: kinetic and equilibrium studies, *J. Environ. Prot.*, 8 (2017) 215–230.
- [34] N.C. Corda, M.S. Kini, A review on adsorption of cationic dyes using activated carbon, *MATEC Web Conf.*, 144 (2018), doi: 10.1051/mateconf/201814402022.
- [35] M.R. Ahmed, H. Al-Aoh, Promising adsorption studies of bromophenol blue using copper oxide nanoparticles, *Desal. Water Treat.*, 139 (2019) 360–368.
- [36] E. Sharifpour, E.A. Dil, A. Asfaram, M. Ghaedi, A. Goudarzi, Optimizing adsorptive removal of malachite green and methyl orange dyes from simulated wastewater by Mn-doped CuO-nanoparticles loaded on activated carbon using CCD-RSM: mechanism, regeneration, isotherm, kinetic, and thermodynamic studies, *Appl. Organomet. Chem.*, 33 (2019), doi: 10.1002/aoc.4768.
- [37] D. Balarak, J. Jaafari, G. Hassani, Y. Mahdavi, I. Tyagi, S. Agarwal, V.K. Gupta, The use of low-cost adsorbent (Canola residues) for the adsorption of methylene blue from aqueous solution: isotherm, kinetic and thermodynamic studies, *Colloid Interface Sci. Commun.*, 7 (2015) 16–19.
- [38] A.A. El-Bindary, H.A. Kiwaan, A.F. Shoair, A.R. Hawas, A novel crosslinked amphoteric adsorbent thiourea formaldehyde calcium alginate: preparation, characterization and adsorption behaviors of removing color from acidic and basic dyes, *Desal. Water Treat.*, 151 (2019) 145–160.
- [39] S. Sehar, F. Sher, S. Zhang, U. Khalid, J. Sulejmanovic, E.C. Lima, Thermodynamic and kinetic study of synthesised graphene oxide-CuO nanocomposites: a way forward to fuel additive and photocatalytic potentials, *J. Mol. Liq.*, 313 (2020), doi: 10.1016/j.molliq.2020.113494.
- [40] A. Özcan, A.S. Özcan, Adsorption of Acid Red 57 from aqueous solutions onto surfactant-modified sepiolite, *J. Hazard. Mater.*, 125 (2005) 252–259.
- [41] A.S. Özcan, S. Tetik, A. Özcan, Adsorption of acid dyes from aqueous solutions onto sepiolite, *Sep. Sci. Technol.*, 39 (2005) 301–320.
- [42] A.S. Özcan, A. Özcan, Adsorption of acid dyes from aqueous solutions onto acid-activated bentonite, *J. Colloid Interface Sci.*, 276 (2004) 39–46.